nature communications

Article

https://doi.org/10.1038/s41467-025-65729-5

Origin of Earth's hydrogen and carbon constrained by their core-mantle partitioning and bulk Earth abundance

Received: 19 September 2024

Accepted: 22 October 2025

Published online: 21 November 2025

Check for updates

Yutaro Tsutsumi[1], Naoya Sakamoto[2], Kei Hirose[1,3] ✉, Shuhei Mita[1], Shunpei Yokoo[1], Han Hsu[4] & Hisayoshi Yurimoto[2,5]

Hydrogen and carbon concentrations in the Earth's core are yet known. Here we determined their metal/silicate partition coefficients (D) simultaneously under typical conditions of core formation and found that D_H and D_C diminish in the presence of carbon and hydrogen, respectively, because of strong interactions between hydrogen and carbon in liquid metal, being markedly different from those separately examined in earlier experiments. With these partitioning data, we investigated the core and bulk Earth abundances of hydrogen and carbon based on core formation scenarios that are compatible with the bulk silicate Earth composition and the mass fraction and density of the core. The modelling results indicate that the Earth building blocks do not match enstatite chondrites in water abundance but require contributions by carbonaceous chondrites. The multi-stage core formation models combined with an Earth accretion scenario accounting for isotopic composition show 0.18–0.49 wt% H and 0.19–1.37 wt% C in the core, leading to 0.53–1.40 wt% H_2O (present as H in the core) and 0.07–0.44 wt% C in the bulk Earth. Our modelling also demonstrates that up to 53% and 72% of Earth's water (hydrogen) and carbon, respectively, could have been derived from non-carbonaceous chondritic materials.

Hydrogen and carbon are important volatile elements on our planet, and their sources[1,2] and the timing[3] of the delivery to the growing Earth are of great interest. Since both hydrogen[4] and carbon[5,6] are known to be strongly siderophile (iron-loving) under high pressure and temperature (P-T), the core is likely to be their largest reservoir. Indeed, the Earth's outer core exhibits a large density deficit with respect to pure iron[7], indicating the presence of substantial amounts of light impurity elements, but the core concentration of each light element has been controversial[8]. In addition to their bulk silicate Earth (BSE) abundances[9,10], understanding the hydrogen and carbon inventories of the core is essential to estimate their bulk Earth contents, which may suggest their origins.

The hydrogen and carbon contents in the core can be constrained by a combination of their metal/silicate partition coefficients under high P-T conditions of core formation and their BSE abundances, including the ocean water. The metal-silicate partitioning of hydrogen has been examined by experiments[4] to 60 GPa and 4560 K as well as by theoretical calculations[11,12]. The partitioning of carbon has been extensively studied below 25 GPa in large-volume presses[13–17] and to 71 GPa in pressure and 5200 K in temperature by laser-heated diamond-anvil cell (DAC) techniques[5,6]. However, these two earlier DAC works reported apparently inconsistent results, although experiments were conducted at similar P-T conditions.

Here, we examined the metal-silicate partitioning of hydrogen and carbon simultaneously in a DAC based on a combination of synchrotron X-ray diffraction (XRD) measurements at high pressure and the textural and compositional analyses on recovered samples by secondary ion mass spectrometry (SIMS) and field-emission-type

[1]Department of Earth and Planetary Science, The University of Tokyo, Bunkyo, Tokyo, Japan. [2]Institute for Integrated Innovations, Hokkaido University, Sapporo, Hokkaido, Japan. [3]Earth-Life Science Institute, Institute of Science Tokyo, Meguro, Tokyo, Japan. [4]Department of Physics, National Central University, Taoyuan City, Taiwan. [5]Department of Natural History Sciences, Hokkaido University, Sapporo, Hokkaido, Japan. ✉e-mail: kei@eps.s.u-tokyo.ac.jp

https://doi.org/10.1038/s41467-025-65729-5

Table 1 | Experimental conditions and results

Run #	Pressure (GPa)	Temperature (K)	Duration (second)	Starting materials	fO_2 (ΔIW)	*nbo/t*	$D_H^{metal/silicate}$		$D_C^{metal/silicate}$	
1	42 (4)	3940 (200)	10	w01+Fe-4wt%C	−1.74	3.51	0.7	(2)	27	(8)
2	55 (6)	4760 (240)	10	w03+Fe-4wt%C	−1.31	1.69	26.1	(63)	132	(53)
3	56 (6)	3800 (190)	9	w02+Fe-4wt%C	−1.36	1.74	8.2	(11)	49	(12)
4	56 (6)	4130 (210)	10	w01+Fe-4wt%C	−1.76	0.82	6.3	(19)	36	(23)
5	55 (5)	3630 (180)	30	w01+Fe-4wt%C	−1.78	0.90	3.1	(8)	41	(8)
6	33 (3)	4060 (200)	10	n02+Fe-4wt%C	−1.25	1.46			84	(25)
7	43 (4)	3930 (200)	10	n01+Fe-4wt%C	−0.93	1.77			77	(35)
8	41 (4)	3660 (180)	10	n02+Fe-4wt%C	−1.26	1.01			141	(62)
9	46 (5)	3980 (200)	60	n02+Fe-4wt%C	−2.09	0.51			369	(324)
10	54 (5)	4060 (200)	4	n01+Fe-4wt%C	−0.60	2.24			14	(4)

D_H and D_C are based on molar concentrations. Numbers in parentheses indicate one standard deviations in the last digits.

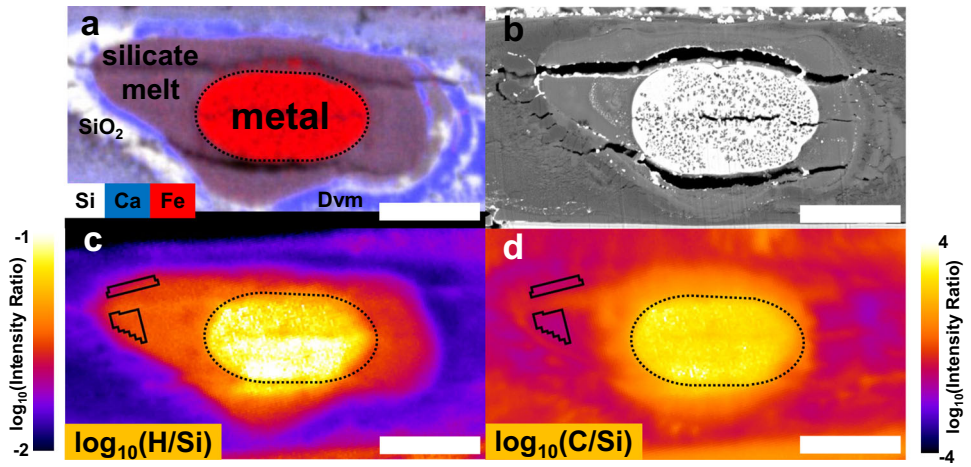

Fig. 1 | Sample cross-section from run #1. a Combined X-ray maps of Si (white), Ca (blue), and Fe (red), showing quenched liquid metal, silicate melt, $CaSiO_3$ davemaoite (Dvm,) and the SiO_2 phase. **b** Back-scattered electron (BSE) image. The SCAPS images of secondary ions intensity ratios of H/Si and C/Si. The H and C contents in silicate melt were determined from the regions of interest (ROIs, enclosed by black lines in (**c**, **d**)) in an area free from the lens-flare effects of the secondary ion optics (see Supplementary Fig. 16 and "Methods") and metal blobs (see the BSE image in (**b**)). A quenched metal portion in (**c**) and (**d**) is from the X-ray map in (**a**). Note that **a**, **c**/**d**, and **b** are slightly different cross sections because of sputtering by the SIMS ion beam and repolishing with a focused ion beam in between. Scale bar, 10 μm.

electron probe microanalyzer (FE-EPMA). With these partitioning data, we modelled the Earth's accretion and core formation processes that account for the BSE composition and the mass and density deficit of the core, which give core concentrations of hydrogen and carbon and accordingly their bulk Earth abundances. These results suggest that the core is a predominant reservoir for both hydrogen and carbon on Earth. We also found that non-carbonaceous chondritic materials could be an important source of the Earth's water and carbon.

Results

Ten separate melting experiments were performed at 33–56 GPa and 3630–4760 K, corresponding to typical conditions of Earth's core formation[18–20] under both hydrous and anhydrous conditions (Table 1). After melting at high pressures, all samples were recovered from a DAC and examined for melting texture and chemical composition on their cross sections at the centre of a heated area (Fig. 1). Quenched liquid metal was found at the central portion, being surrounded by silicate melt. The davemaoite ($CaSiO_3$-perovskite) and SiO_2 layers were present outside of the silicate melt pool, which is consistent with the XRD observations during melting (Fig. 2). The further outside, colder region was under subsolidus temperatures.

Partitioning of hydrogen

The metal/silicate partition coefficients of hydrogen, $D_H^{metal/silicate}$ were obtained as:

$$D_H^{metal/silicate} = \frac{x'^{metal}_H}{x^{silicate}_{HO_{0.5}}} \quad (1)$$

where x'^{metal}_H and $x^{silicate}_{HO_{0.5}}$ represent the molar fractions of hydrogen in metal and silicate, respectively (see Eq. 10 for x'^{metal}_i in "Methods"). The D_H values obtained in this study in the presence of carbon ranged from 0.7 to 26.1 (Table 1), notably lower than the $D_H^{metal/silicate}$ = 22–46 measured in a carbon-poor system by previous DAC experiments[4].

The metal-silicate partitioning of hydrogen can be expressed as a chemical reaction:

$$HO_{0.5}^{silicate\ melt} + \frac{1}{2}Fe^{metal} = H^{metal} + \frac{1}{2}FeO^{silicate\ melt} \quad (2)$$

The exchange coefficient K_D for this reaction is parameterized as functions of P and T with regression constants a, b, c and d:

$$\log_{10}K_D = \log_{10}\frac{x'^{\text{metal}}_H}{x^{\text{silicate}}_{HO_{0.5}}}\cdot\sqrt{\frac{x^{\text{silicate}}_{FeO}}{x'^{\text{metal}}_{Fe}}} = \log_{10}\frac{x'^{\text{metal}}_H}{x^{\text{silicate}}_{HO_{0.5}}} + \frac{1}{4}\Delta IW =$$
$$\log_{10}D_H^{\text{metal/silicate}} + \frac{1}{4}\Delta IW = a + \frac{b}{T} + c\cdot\frac{P}{T} + d\cdot\log_{10}\left(1 - x'^{\text{metal}}_C\right) \quad (3)$$

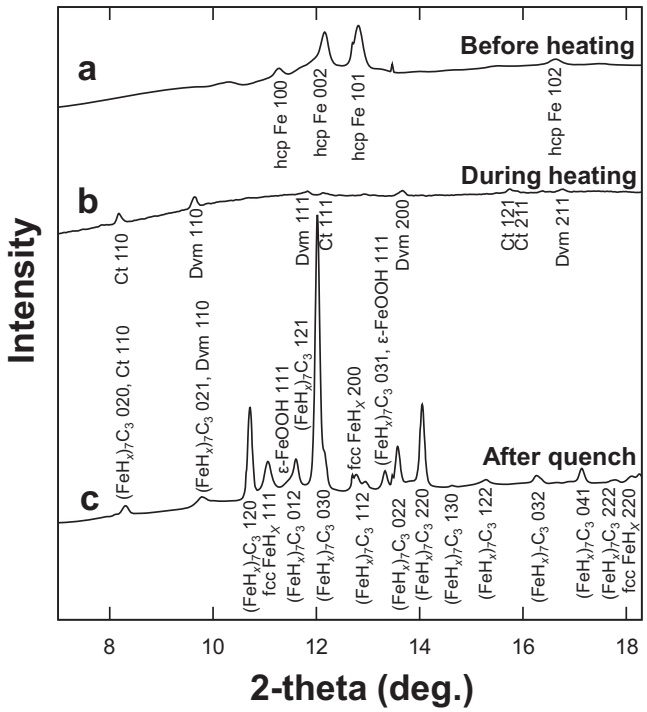

Fig. 2 | XRD patterns obtained in the high-pressure melting experiment. They were collected before (**a**), during (**b**) and after heating (**c**) to 3940 K at 42 GPa in run #1. During heating, XRD peaks were observed only from Dvm and $CaCl_2$-type SiO_2 (Ct), which were present outside of a silicate melt pool (see Fig. 1a), indicating the melting of both metal and silicate. After quenching temperature, the peaks from fcc FeH_x, ε-FeOOH, and $(FeH_x)_7C_3$ appeared. The amount of hydrogen in liquid metal was estimated from the phase proportion and hydrogen concentrations in these quench crystals. See text for details.

in which x'^{metal}_C is the molar fraction of carbon in liquid metal (Eq. 10), and $d\cdot\log_{10}\left(1 - x'^{\text{metal}}_C\right)$ approximates a non-ideal interaction between H and C[5,21]. Following previous studies[4,22], oxygen fugacity fO_2 relative to the iron-wüstite (IW) buffer is approximated as $\Delta IW \approx 2\log_{10}\left(x^{\text{silicate}}_{FeO}/x'^{\text{metal}}_{Fe}\right)$, which was obtained from the EPMA analyses. Fitting Eq. 3 to the present and earlier data[4] yields $a = 2.31(20)$, $b = -1542(500)$, $c = -38.9(78)$ and $d = 6.69(30)$. Fig. 3a shows the negative pressure and positive temperature dependence of K_D for the partitioning of hydrogen after correcting for the effect of carbon, consistent with the results of Tagawa et al[4]. We note that carbon in liquid metal strongly reduces $D_H^{\text{metal/silicate}}$ (Fig. 3b). All of the experimental data obtained in this study and Tagawa et al[4]. are well reproduced by Eq. 3 (Supplementary Fig. 1a).

Partitioning of carbon

Similarly, the metal/silicate partition coefficients for carbon $D_C^{\text{metal/silicate}}$ were also calculated as:

$$D_C^{\text{metal/silicate}} = \frac{x'^{\text{metal}}_C}{x^{\text{silicate}}_C} \quad (4)$$

The D_C ranged from 14 to 369 in the hydrogen (water)-free system and from 27 to 132 in the hydrogen (water)-bearing system (Table 1). We fitted the following equation to the present results combined with earlier DAC data[5,6] and low P-T data obtained for silicate melts with the ratio of nonbridging oxygens to tetrahedrally coordinated cations (nbo/t) less than 10 from multi-anvil and piston-cylinder experiments[13–15,17] that were performed in carbon-undersaturated systems:

$$\log_{10}D_C = a + b\cdot\Delta IW + c\cdot nbo/t + d\cdot\log_{10}\left(1 - x'^{\text{metal}}_H\right) \quad (5)$$

in which ΔIW represents oxygen fugacity relative to the iron-wüstite buffer. The fitting provides $a = 1.51(30)$, $b = -0.68(15)$, $c = -0.33(7)$, and $d = 1.76(77)$, showing the strong negative effects of oxygen fugacity, nbo/t, and hydrogen concentration in liquid metal on D_C (see Fig. 4a–c, respectively). Note that metal compositions were calculated as x'^{metal}_i also for the previous experimental data.

Considering the effects of oxygen fugacity and nbo/t, all of these earlier experimental data are well reproduced by Eq. 5 (Supplementary Fig. 1b). The P and T dependence of D_C is not explicit in Eq. 5 unlike previous DAC studies[5,6] (Supplementary Fig. 2). The low P-T data used together with the high P-T DAC data are key to clarifying such P and T effects; in contrast to earlier DAC studies[5,6], we did not employ data obtained in a graphite capsule, which causes carbon saturation in

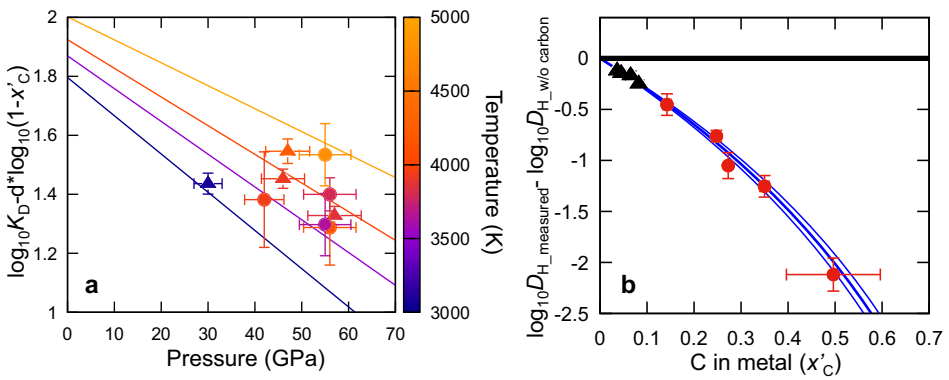

Fig. 3 | Partitioning of hydrogen. a Pressure and temperature dependence of the exchange coefficient K_D for metal-silicate partitioning of hydrogen after correcting for the effect of carbon (Eq. 3). Blue (3000 K), purple (3500 K), orange (4000 K), and yellow lines (5000 K) show isotherms. **b** Reduction in metal/silicate partition coefficient D of hydrogen (molar basis) as a function of carbon concentration in liquid metal. Circles, this study; triangles, Tagawa et al[4]. Error bars represent one standard deviation.

https://doi.org/10.1038/s41467-025-65729-5

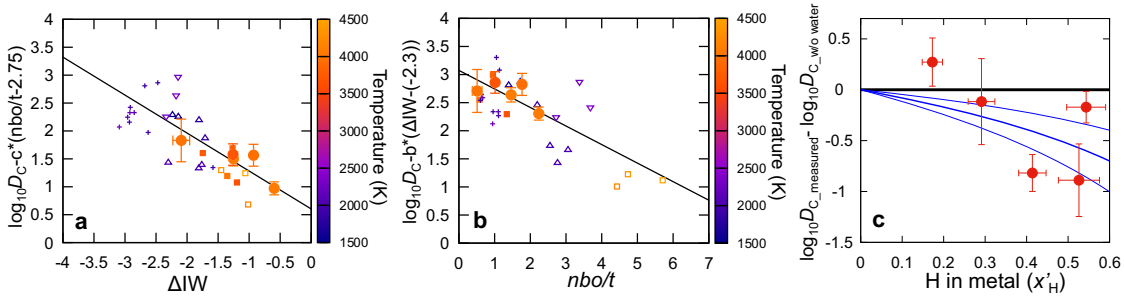

Fig. 4 | Partitioning of carbon. Partition coefficient D of carbon (molar basis) as a function of ΔIW (**a**) and *nbo/t* (**b**) obtained in hydrogen-free experiments and of hydrogen concentration in metal (**c**). See Eq. 5. Colour indicates temperature. Circles, this study; squares, Blanchard et al[6]. (closed) and Fischer et al[5]. (open); triangles, Fichtner et al[17]. (normal) and Dasgupta et al[13]. (inverted); crosses, Kuwahara et al[14,15]. Error bars represent one standard deviation.

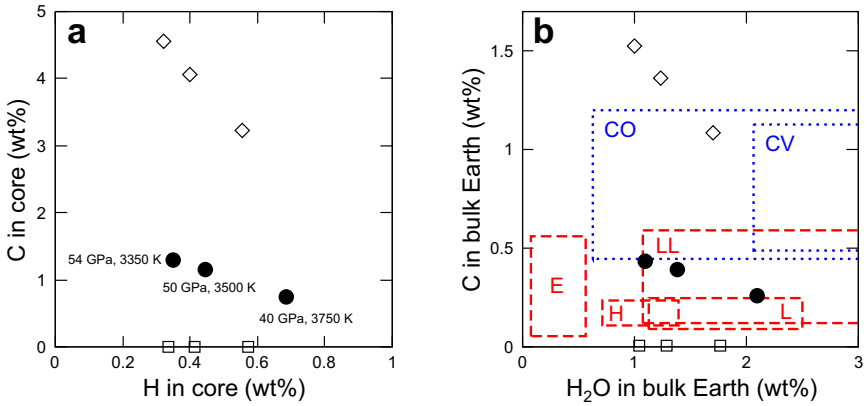

Fig. 5 | Modelling of single-stage core formation. Hydrogen (water) and carbon concentrations in the core (**a**) and the bulk Earth (**b**) considering the *P-T* conditions of core metal segregation at 40 GPa and 3750 K[18], 50 GPa and 3500 K[19], and 54 GPa and 3350 K[20]. Black circles, calculated using D_H and D_C simultaneously determined in this study; diamonds, D_H from Tagawa et al.[4] and D_C from Blanchard et al.[6]; squares, D_H from Tagawa et al.[4] and D_C from Fischer et al.[5] Red and blue regions in **b** indicate H_2O and C concentrations in non-carbonaceous and carbonaceous chondrites, respectively. See Supplementary Table 8 for the H_2O and C contents in each type of chondrite.

silicate melts, since saturation changes the partitioning behaviours[14,15]. Li et al.[16] also did not find the P and T effects on D_C when ΔIW < −1.5. In addition, it has been reported[14,16] that the solubilities of carbon in metallic liquid and silicate melt do not depend on pressure. Since the chemical potential of C in a carbon-saturated phase is identical to that in graphite/diamond, it suggests that the pressure dependence of chemical potentials of C is similar among these molten phases and graphite/diamond, and therefore the molar volumes of C in metallic liquid and silicate melt are close to each other, supporting the small pressure dependence of D_C (i.e., small volume change in the reaction).

Discussion

Single-stage core formation model

The single-stage core formation model is conceptually simple, assuming that the entire core and mantle reached chemical equilibrium under a certain P, T, and fO_2 condition. Such a condition has been estimated, based on the metal-silicate partitioning of moderately siderophile elements, to be 40 GPa and 3750 K (ref. 18), 50 GPa and 3500 K (ref. 19), or 54 GPa and 3350 K (ref. 20) (Supplementary Table 1), and ΔIW = −2.3. The BSE water abundance may be 710 ppm[23], including 1.6×10^{24} g water in the crust, ocean, and atmosphere[24], while the higher BSE water contents of 1760 ppm and 1070 ppm H_2O have also been proposed[25,26]. On the other hand, the carbon abundance in the BSE may be 120 ppm[27], 140 ppm[23] or ~160 ppm (or ~220 ppm)[28].

Based on the 710 ppm H_2O (ref. 23) and 120 ppm C (ref. 27) in the BSE, we can calculate core concentrations of hydrogen and carbon by using D_H and D_C at the conditions of core-mantle chemical equilibrium (core formation). Following the single-stage core formation model proposed by Wade and Wood[18], Eqs. 3 and 5 showed 0.68 wt% H and 0.75 wt% C in the core with $D_H = 92$ and $D_C = 67$ (Fig. 5a, Supplementary Table 1), in which we employed $nbo/t = 2.75$ that is for a pyrolitic mantle composition[29], fixed the S content to be 2 wt% in the core from cosmochemical and geochemical constraints[27] and calculated the core abundances of Si and O using their metal-silicate partitioning data[18]. Also, similar calculations based on other core formation model[19], including the metal/silicate partition coefficients of Si and O, found 0.45 wt% H and 1.15 wt% C in the core ($D_H = 56$ and $D_C = 96$) (Supplementary Table 1). The Fischer et al.'s[20] model provides 0.35 wt% H and 1.29 wt% C with $D_H = 44$ and $D_C = 107$.

These results suggest that the core is a primary reservoir for both hydrogen and carbon; >98% and >97% of their bulk Earth budgets may be present in the core, respectively. We also note that when we employ the separately-determined D_H (ref. 4) and D_C values[5,6] without considering the strong interaction between hydrogen and carbon, the C content in the core is calculated to be much higher[6] or lower[5] than described above, while H concentration is similar (Fig. 5a). Such core abundances indicate 1.10–2.08 wt% H_2O and 0.26–0.44 wt% C in the bulk Earth (Fig. 5b, Supplementary Table 1), which corresponds to Earth's building blocks if we do not consider volatile loss during accretion.

Homogeneous accretion & multi-stage core formation model

The multi-stage core formation models may be more realistic scenarios in which the core grows stepwise during the Earth accretion[3]. Here we employ all of the nine multi-stage core formation models reported by Tagawa et al.[4], where the Earth grows by 1000 steps upon accretion

https://doi.org/10.1038/s41467-025-65729-5

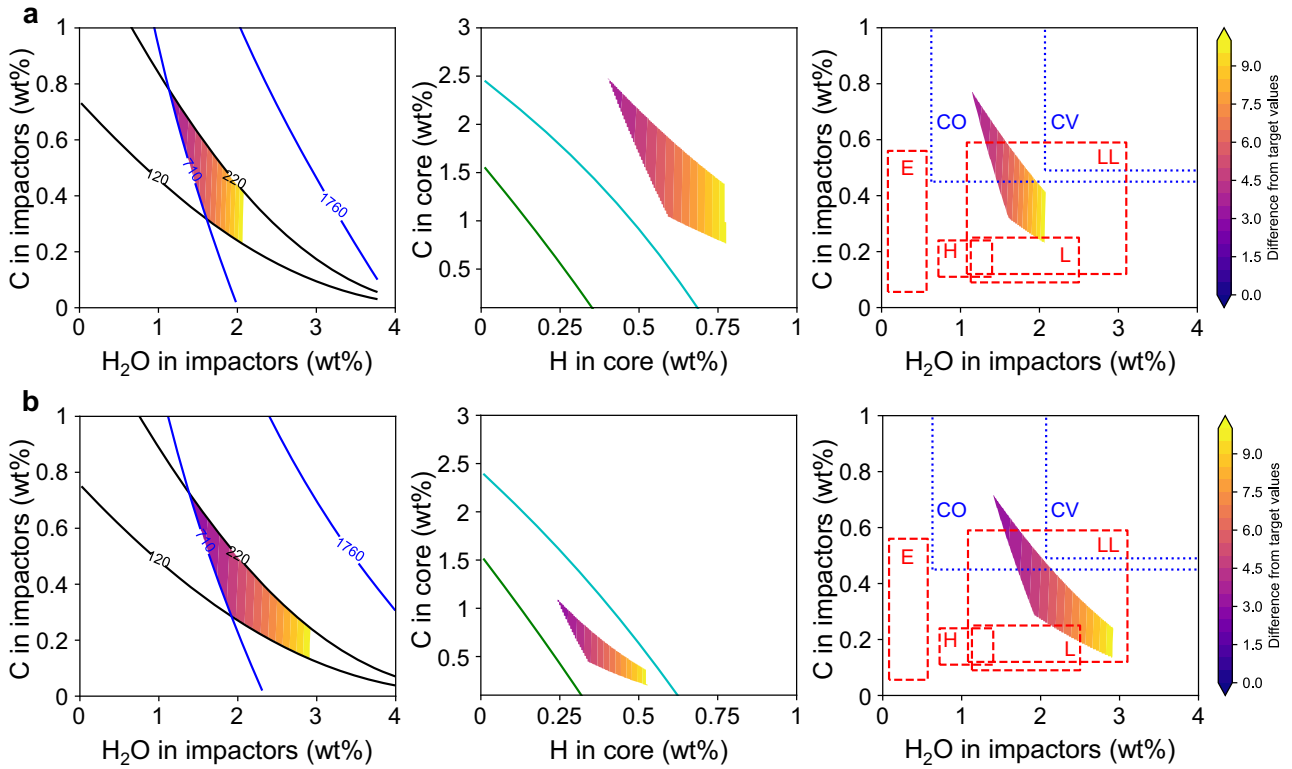

Fig. 6 | Modelling of homogeneous accretion & multi-stage core formation (model S1). The delivery of water and carbon to the Earth is considered from the beginning (**a**) and only after 50% accretion (**b**). The coloured region in the left panels indicates H_2O and C concentrations in impactors, explaining the BSE abundances of 710–1760 ppm H_2O and 120–220 ppm C in addition to the core mass fraction and the mantle FeO, Ni and Co contents (colour indicates the deviation from target values). Those in the central panels show the corresponding H and C contents in the core, which are compared with H and C concentrations required to explain the outer core density deficit when T_{ICB} = 5400 K (green curve) and 4800 K (right blue curve) (see text). The H_2O and C abundances in impactors (=Earth building blocks) are compared to those in non-carbonaceous (red region) and carbonaceous chondrites (blue region) in the right panels.

of impactors that are identical in size and composition. These models explain ~700 ppm H_2O in the BSE, including the ocean water and the mantle FeO, NiO and CoO contents based on their metal/silicate partition coefficients[3,19,20,30], as well as the Earth's core mass fraction. In this study, we additionally examine the distributions of carbon with the newly determined D_H and D_C that consider the effect of their strong interactions (Eqs. 3 and 5).

We explored impactor H_2O and C concentrations, which lead to the amounts of residual water and carbon in silicate being both within the range of existing estimates of the present-day BSE concentrations of 710–1760 ppm H_2O (refs. 23–26) and 120–220 ppm C (refs. 23,27,28) at the end of accretion. The total difference in mantle concentrations of FeO, NiO and CoO (ref. 31) and core mass fraction between the modelling results and the target values is defined as:

$$\sigma = \sqrt{1/4 \times \sum \left\{ \frac{(\text{caluculated value}) - (\text{present Earth value})}{(\text{error of the present Earth value})} \right\}^2} \quad (6)$$

We suppose that a model explains the core size and the BSE composition reasonably well when $\sigma < 10$. Each model (S1–S3, F1–F3 and R1–R3 models)[4] gives the specific P-T evolution of metal-silicate chemical equilibrium, impactor size (=the Earth size divided by $N \times 1000$), impactor bulk (silicate + core) composition (Supplementary Table 2) and exchange coefficients for Ni, Co, O and Si. Here we fixed Φ_{Fe} (metallic Fe/total Fe) = 0.987 and Φ_{Si} (metallic Si/total Si) = 0.034, unlike Tagawa et al[4].'s simulations, by considering the core-mantle partitioning of O and Si in an enstatite-chondrite-like impactor[32] at 1 bar and 2023 K (ref. 29) using their partition coefficients[30].

We searched for the sets of P_{final} (the pressure of core metal segregation at the final step of accretion) and impactor water and carbon concentrations, which minimize the σ value (Eq. 6) while satisfying the residual 710–1760 ppm H_2O and 120–220 ppm C in the BSE. For each of the nine models, we found a σ minimum with specific P_{final} (Supplementary Fig. 3). With such P_{final} values, the present homogeneous multi-stage core formation models show that accreting identical impactors with 0.2–2.4 wt% H_2O and 0.2–1.0 wt% C accounts for the BSE composition (FeO, NiO, CoO, H_2O and C contents) and the Earth's core size (Fig. 6a and Supplementary Fig. 4); typical examples of their evolutions during accretion are given in Supplementary Fig. 5. However, the total amount of light impurity elements in the core at the end of the Earth accretion (the calculated core concentrations of H, C, Si and O + assumed 2 wt% S, see Supplementary Fig. 5) are more than required to explain the present-day outer core density deficit[33] (Fig. 6a and Supplementary Fig. 4) even when the temperature at the inner core boundary (ICB) is relatively low (T_{ICB} = 4800 K) and the core liquid is saturated with Si + O under corresponding 3500 K at the core-mantle boundary[34] (note that low T_{ICB} and the SiO_2 crystallization from the liquid core leave relatively large room for hydrogen and carbon). It is therefore unlikely from the present modelling that the Earth's building blocks included water and carbon from the beginning of accretion.

Next, we examined alternative scenarios in which water and carbon were delivered in a late stage of the Earth's accretion. Such a late delivery of volatiles has been considered for sulphur in a previous multi-stage core formation model[35–37]. In the case of their delivery after 50% accretion (Supplementary Figs. 6–8), the calculated total amount of the core light elements (0.1–0.6 wt% H, 0.1–1.5 wt% C, Si and O contents and assumed S abundance) explains the present-day core density deficit when T_{ICB} is between 5400 K and 4800 K, taking the Si + O saturation and resulting SiO_2 crystallization upon core cooling into account[34] (Fig. 6b and Supplementary Fig. 7). These models require

https://doi.org/10.1038/s41467-025-65729-5

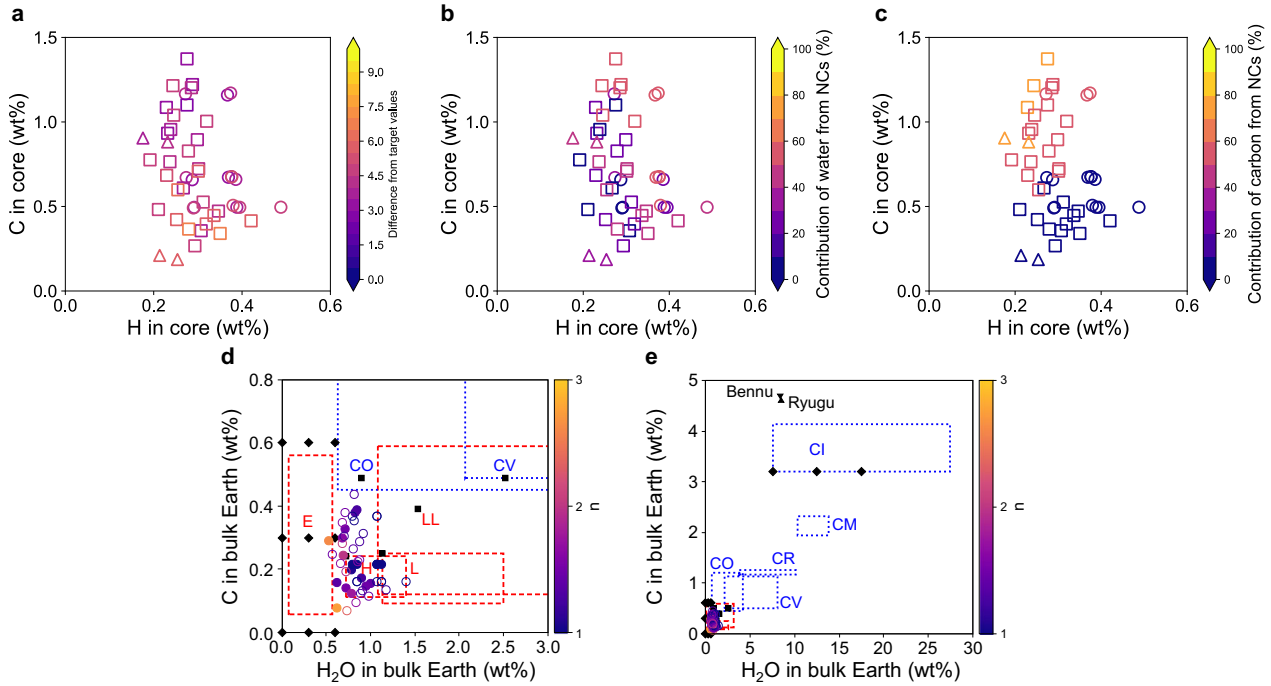

Fig. 7 | Modelling of heterogeneous accretion & multi-stage core formation. Water and carbon are delivered according to the 4-stage accretion scenario by Dauphas et al.[41] that explains Earth's isotopic composition. **a**–**c** Modelling results on core H and C concentrations (circles, $n = 1$; squares, $1 < n < 2$; triangles, $2 < n < 3$). Colours indicate difference from target values (σ) (**a**) and the fraction of NC-type materials as sources for Earth's water (**b**) and carbon (**c**). **d**, **e** The bulk Earth H_2O (present as H in the core) and C abundances compared to those in each type of chondrite (Supplementary Table 8), including the Ryugu[71] and Bennu[72] samples. The dependence on n is indicated by colour. Closed and open symbols consider none and 25% loss of carbon during Earth accretion, respectively. Diamonds and squares show the variations in H_2O and C concentrations in E-/CI-type materials (varied in each model) and other types (fixed), respectively, employed in our modelling, while the reported ranges of the H_2O and C contents for NC and CC materials are indicated by boxes with broken and dotted lines, respectively.

>1 wt% H_2O and <1 wt% C in the impactors during the latter half of the accretion in most models. Their typical evolutions are illustrated in Supplementary Fig. 8 for the S1 model showing relatively small σ values when the volatile-rich latter half impactors include 2.0 wt% H_2O and 0.4 wt% C (leading to 1.0 wt% H_2O and 0.2 wt% C in the bulk Earth) (Supplementary Table 3). This specific scenario finds 0.35 wt% H and 0.62 wt% C in the core, indicating that >95% of the bulk Earth budgets of both hydrogen and carbon may be present in the core.

Heterogeneous accretion & multi-stage core formation model

It is highly likely that the Earth was formed from a variety of different types of chondritic materials. Indeed, isotopic compositions, in particular Mo (ref. 38), Ru (ref. 39) and Zr isotopes[40], suggest that the Earth's building blocks are close to enstatite (E)-chondrite-type materials but involve some carbonaceous chondrites (CCs) that are classified into CI, CM, CR, CO and CV (Supplementary Table 8). The recent isotopic mixing model by Dauphas et al. [41] proposed accretion scenarios to account for the Earth's isotopic composition, showing the proportions and delivery timing of E-, CI-, and minor amounts of ordinary (O) chondrites (H, L, and LL) and other carbonaceous (CO + CV) chondrites. Their 4-stage model argued that water- and carbon-rich CC-type materials accreted to our planet mainly in the last 25% accretion, broadly consistent with our modelling described above. Here, the Dauphas et al.'s[41] 4-stage accretion scenario was combined with our multi-stage core formation model (model S1[4] in the previous section) such that the model is constrained not only by the BSE elemental composition and the core mass and density deficit but also by the isotopic composition. Furthermore, we also examined the effects of impactor size that changes the efficiency of chemical equilibrium between impactor metal and proto-Earth silicate[4,42] (by varying the number of steps for Earth accretion, $N \times 1000$), differentiation of impactors before accreting to the Earth (by including volatile-free impactors with a frequency of 1-1/n) and volatile loss on Earth.

Considering the wide ranges of 1) the reported H_2O and C contents in E- and CI-chondrite-type materials[2,43–47] (Fig. 7d, e, Supplementary Table 8, Supplementary Fig. 9), 2) $N = 1$–10 (Supplementary Fig. 10) and 3) $n = 1$–8 (Supplementary Fig. 11) along with 4) none or 25% carbon loss throughout the Earth accretion (water/hydrogen loss may have been minor)[48,49], we looked for the sets of these parameters that find $\sigma < 10$ through the search for P_{final} and 710–1760 ppm H_2O and 120–220 ppm C in the BSE. Consequently, these modellings show 0.18–0.49 wt% H and 0.19–1.37 wt% C in the core (Fig. 7a). Such core concentrations give 0.53–1.40 wt% H_2O (present as H in the core) and 0.07–0.44 wt% C in the bulk Earth (Fig. 7d). We note that these ranges of the core and bulk Earth H (H_2O) and C contents are similar to those obtained by the homogeneous accretion & multi-stage core formation modelling shown above that is based on the model S1 same as here and considers the delivery of water and carbon only after 50% accretion (Fig. 6b). In addition, in almost all cases, the parameter sets that satisfy the BSE composition and the Earth's core size ($\sigma < 10$) provide the total amount of the core light elements accounting for the core density deficit with $T_{ICB} = 4800$–5400 K.

The 0.19–1.37 wt% C in the core obtained in these simulations is higher than the core C concentrations of ~0.1–0.2 wt% reported by Blanchard et al.[6] and Fischer et al.[5], in which the effect of hydrogen on D_C was not taken into account. It is because the C abundance in the core is almost independent of the D_C in the Blanchard et al.'s[6] model although they used a higher D_C. The D_C utilized in the modelling by Fischer et al.[5] is the extrapolated one and lower than that applied in this study. Note that the present parameterization of D_C is consistent with the experimental data by Fischer et al.[5] but employs more data including those by Blanchard et al.[6] and this study. In addition, some recent simulations[48,49] included atmosphere as an additional reservoir, which is

important in particular for C, but it reduces the calculated core H and C contents only by less than ~5% in the present modelling (Supplementary Fig. 12) since impactor metal reaches chemical equilibrium with a limited portion of an existing magma ocean[42]. Indeed, the Earth accretion and concurrent core formation must have been complicated processes, for which too few constraints are available so far. The present modelling of core composition employed the BSE isotopic composition and the core density deficit as additional constraints, neither of which has been used in earlier simulations. It is noted, however, that the possible ranges of the core H and C abundances demonstrated in this study are still dependent on model assumptions such as the limited efficiency[4] of chemical equilibrium between impactor metal and proto-Earth silicate. This assumes that upon each impact, the timescale of the metal migration to the core is shorter than that of the compositional homogenization of the entire magma ocean[42].

Origins of Earth's water and carbon

All of these modellings show that the bulk Earth H_2O (incorporated as H in the core) abundance is higher than that of E-chondrites—in other words, E-chondrites alone cannot be the source of Earth's water (Figs. 5b, 6b and 7d). Furthermore, the heterogeneous multi-stage core formation models show that 1 to 53% of Earth's water may have derived from the non-carbonaceous (NC)-type materials (E- + O-chondrites) and the rest was from the CC-type ones that constitute 7% of the total Earth building blocks[41] (Fig. 7b). Also, 2 to 72% of the Earth's carbon could have originated from the NC-type materials with/without taking 25% loss during accretion into account[48,49] (Fig. 7c), strongly depending on carbon concentration in E-chondrites. We also note that 3–10% and 3–24% of the BSE H_2O and C budgets, respectively, were derived by the late veneer, the additional 0.5% accretion after the core formation[41]. It suggests that the majority of Earth's hydrogen and carbon were involved in metal-silicate partitioning, which causes isotopic fractionation, leaving their isotopic ratios in the BSE different from those of the bulk Earth and Earth building blocks.

Methods

High-pressure melting experiments

Laser-heated DAC techniques were used to generate high *P-T* conditions (Table 1). We prepared five different glasses for silicate starting materials, which have mid-ocean ridge basalt (MORB) compositions with various amounts of H_2O; 1.0 wt% (w01), 0.15 wt% (w02), 0.6 wt% (w03), and none (n01 and n02) (Supplementary Table 4). A thin foil (~7 μm thick) of iron containing 4.0 wt% carbon, same as that employed previously[50], was sandwiched between layers of silicate glass. They were loaded into a 120 μm hole at the centre of a pre-indented rhenium gasket. Diamond anvils with a flat 300 μm culet were used. After loading, for experiments with anhydrous glass starting materials, we put the DAC into a vacuum oven at 400 K for >12 hours to remove moisture on the sample and subsequently compressed the sample in an argon atmosphere to avoid water adsorption. Under high pressure of interest, the sample was heated from both sides with a couple of 100 W single-mode Yb fibre lasers at BL10XU, SPring-8 synchrotron radiation source, with in-situ XRD measurements[51]. XRD patterns were collected before/during/after heating using a monochromatic X-ray beam with an energy of ~30 keV that was focused to a 6 μm area (full width of half maximum) on the sample position. Melting of a sample was confirmed by the disappearance of XRD peaks except weak ones that derived from silicate liquidus phases outside of a silicate melt pool (Fig. 2). Heating duration ranged from 4 to 60 seconds, which is long enough for each element to diffuse in liquid metal[52] and silicate melt[53]. Indeed, both metal and silicate were found to be homogeneous in composition in this study, except for heterogeneous distributions of small metallic blobs in the silicate melt pool (Fig. 1b). It has been demonstrated by earlier experiments using a multi-anvil press that molten metal and silicate melt reached chemical equilibrium in such a heating time scale[54]. Considering the much smaller sample size and higher temperatures in the present DAC study than in the multi-anvil experiments, the time necessary for chemical equilibration should be shorter. Temperature was measured by a spectro-radiometric method[51]. Pressure was measured based on the Raman shift of a diamond anvil at 300 K after heating[55] and corrected for thermal pressure contributions that have been estimated to be +2.5 GPa per 1000 K (refs. 4,56). The errors in pressure and temperature may be ±10% and ±5%, respectively[57].

XRD and EPMA analyses of liquid metal

The hydrogen contents in liquid iron were estimated from XRD data collected at high pressures and 300 K, since the iron sample loses hydrogen when it transforms into the body-centred cubic structure[4,58]. The XRD patterns showed the appearance of face-centred-cubic (fcc) FeH_x and hydrogen-bearing $(FeH_x)_7C_3$ [or $(FeH_x)_3C$] formed from liquid metal upon quenching temperature (Fig. 2c). Their lattice volumes were larger than those of pure fcc Fe and Fe_7C_3 (or Fe_3C) at equivalent pressure and 300 K, respectively[59–61], which is attributed to the incorporation of hydrogen into their interstitial sites. Following Tagawa et al[4]., the hydrogen content x was calculated as:

$$x = \frac{V_{FeH_x} - V_{Fe}}{\Delta V_{H\_Fe}} \text{ in } FeH_x \tag{7}$$

$$x = \frac{V_{(FeH_x)_7C_3} - V_{Fe_7C_3}}{\Delta V_{H\_Fe7C3}} \text{ in } (FeH_x)_7C_3 \tag{8}$$

$$x = \frac{V_{(FeH_x)_3C} - V_{Fe_3C}}{\Delta V_{H\_Fe3C}} \text{ in } (FeH_x)_3C \tag{9}$$

where V_{FeHx}, $V_{(FeHx)7C3}$ and $V_{(FeHx)3C}$ represent the observed lattice volume per Fe atom of each phase, and V_{Fe}, V_{Fe7C3} and V_{Fe3C} are from their equations of state[59–61]. ΔV_H represents the volume increase per hydrogen atom. We employed ΔV_{H_Fe} previously reported for fcc Fe[62]. ΔV_{H_Fe7C3} was determined by first-principles calculations in this study (see below for the first-principles calculations section, Supplementary Table 5 and Supplementary Fig. 13). Since hydrogen favours different interstitial sites depending on hydrogen concentration, we calculated x in $(FeH_x)_7C_3$ based on three different ΔV_{H_Fe7C3} applicable to each hydrogen concentration range, $x < 0.14$, $0.14 < x < 0.29$ and $0.29 < x < 0.57$ (Supplementary Table 6). We also found that ΔV_H is similar between Fe and Fe_7C_3, in particular $x = 0.22$ and 0.45 observed in $(FeH_x)_3C$ at 45–47 GPa and 300 K (Supplementary Table 6 and Supplementary Fig. 13), and therefore used ΔV_{H_Fe7C3} to calculate x in $(FeH_x)_3C$. In all runs, fcc FeH_x, ε-FeOOH and $(FeH_x)_7C_3$ [or $(FeH_x)_3C$] were found in XRD patterns collected from temperature-quenched liquid. Their hydrogen concentrations x were estimated to be 0.03–1.76, 0.21–0.30, and 0.22–0.45, respectively (Supplementary Table 6). We then calculated the total hydrogen concentration in liquid to be 0.33 to 0.98 wt% (Supplementary Table 7) based on the proportions of these crystals in quenched liquid, which were obtained by mass balance calculations using the FE-EPMA analyses (see below), considering the presence of silicon in the iron site. The incorporation of silicon into Fe increases its unit-cell volume to a minor extent[63]. While 0.16–6.47 wt% Si may be present in these iron and iron carbides in the present experiments (Supplementary Table 7), the estimate of the hydrogen content x is reduced by 0.02 at 50 GPa even when 5.9 wt % Si is included[63].

The carbon contents in quenched metal liquids were obtained based on the electron microprobe analyses on the cross sections of recovered samples. After recovering samples at ambient conditions, sample cross sections at the centre of a laser-heated spot were prepared parallel to the compression/laser-heating axis with a focused ion

beam (FIB, Versa 3D™, FEI). Textural and chemical characterizations were made with an FE-type scanning electron microscope (FE-SEM) and energy dispersive X-ray spectroscopy (EDS). Gold coating was made. We found 3.04–9.51 wt% C in quenched liquid metal along with other major elements with an FE-EPMA (JXA-8530F, JEOL) (Supplementary Table 7). At least five different points were measured for each phase. We employed an acceleration voltage of 12 kV, beam current of 15 nA, and LIF (Fe), TAP (Al, Na), TAPH (Mg), LDE1 (O), LDE2H (C), and PETJ (K, Ca, Si, Ti) as analyzing crystals. The calibration curve for C was obtained with Fe_3C, Fe-0.84 wt% C (JSS066-6, the Japan Iron and Steel Federation), and a rhenium gasket (assumed to be free of carbon) (Supplementary Fig. 14). Fe, Al_2O_3, MgO, Si, SiO_2, TiO_2, $CaSiO_3$, $KTiOPO_4$, and $NaAlSi_3O_8$ were used as standards for other elements. The X-ray counting time for peak/background was 20/10 seconds. The ZAF correction was applied. The major element compositions of silicate melt and the silicate starting materials were also obtained with an FE-EPMA (Supplementary Table 4).

SIMS measurements of silicate melt

We determined the hydrogen (water) and carbon contents in quenched silicate melts with SIMS equipped with a two-dimensional ion detector, stacked CMOS-type active pixel sensor (SCAPS) at the Hokkaido University[4,64–67] (Fig. 1c, d). This system provides quantitative maps of secondary ions emitted from the sample surface because the CMOS sensor exhibits a good linear relationship between an output voltage and the number of secondary ions[66]. Therefore, the abundance of each element from the intensity map can be quantified. The sample cross sections were coated with a ~70 nm thick Au layer by plasma sputtering to compensate for electrostatic charging on the sample surface. We used the Cs^+ primary beam rastered across a 100 µm × 100 µm region on the sample. In order to prevent the effect of electrical charging, analyses were performed while applying electrons with an electron gun. A contrast aperture was set to be 100 µm in diameter, the exit slit was opened fully for $^1H^-$ and 750 µm for others. Pressure during measurement was 2×10^{-7} Pa. The SCAPS images of $^1H^-$, $^{12}C^-$, and $^{28}Si^-$ secondary ions were collected. Accumulation time was 150, 100, and 10 seconds in each image, respectively. We employed five silicate glasses with known H_2O and C concentrations as standards (0.0 to 1.8 wt%, 0.0 to 389 ppm, respectively)[68] and prepared an additional silicate glass standard that contains 1.3 wt% C to fully cover the range of C concentration in silicate melt in the present experiments. Based on these standard glass analyses, we converted intensity ratios, $^1H^-/^{28}Si^-$ and $^{12}C^-/^{28}Si^-$ into mass ratios. The intensity ratios from the secondary ion images are linearly correlated with the mass ratios of H/Si or C/Si of these standards (correlation coefficient $R^2 = 0.997$ and 1.000, respectively, as shown in Supplementary Fig. 15). Water (hydrogen) or carbon concentration in silicate melt was then obtained by multiplying the H/Si or C/Si ratio by the Si content acquired by FE-EPMA. While the silicate melt in run #1 included H_2O much more than 1.8 wt% in the standard glass, each parameter in Eq. 3 for D_H does not change beyond uncertainty when excluding the data from run #1.

Hydrogen distributions were homogeneous in quenched silicate melt (Supplementary Fig. 16), suggesting that hydrogen did not migrate from liquid metal to surrounding silicate upon quenching temperature. The $^{12}C^-$ intensities from metal were higher by more than two orders of magnitude than those from silicate melt (Supplementary Fig. 16). The high C intensity from the metal leaked into the surrounding silicate melt due to the lens-flare or aberration effect. Therefore, the regions of interest (ROIs) in the silicate melts, from which we obtained their hydrogen and carbon abundances, were chosen from an area free from such flare effect from the metal based on the 2D map and line profile of the $\log_{10}$(C) values (Supplementary Fig. 16). In addition, we avoided an area where small metallic blobs are present in the silicate melt. As shown in a back-scattered electron image (Fig. 1b), the outer part of a silicate melt layer is free from the metallic blobs. Following the arguments made in the earlier experiments on metal-silicate partitioning of carbon by Blanchard et al.[6], we interpret that such blobs are not quench products but were present during melting. Indeed, the back-scattered electron image given in Fig. 1b does not show the Fe depletion in areas next to the blobs, which supports that they were not formed from silicate melt upon quenching. The SIMS analyses demonstrate that the amounts of H_2O widely ranged from 0.11 to 10.78 wt% in silicate melts (Supplementary Table 4). Their carbon contents were found to be 0.02–0.60 wt% and 0.008–0.44 wt% when using hydrous and anhydrous silicate starting materials, respectively.

Activities of elements in (H, C)-rich metal and oxygen fugacity

Liquid metals found in this study included carbon (and hydrogen in experiments using H_2O-bearing starting materials). The presence of hydrogen and carbon decreases the molar fraction of iron in metal (x_{Fe}^{metal}), which apparently increases the oxygen fugacity relative to iron-wüstite (IW) buffer, $\Delta IW \sim 2\log_{10}\left(x_{FeO}^{silicate}/x_{Fe}^{metal}\right)$ and changes the exchange coefficient $K_D^O = x_{Fe}^{metal} x_O^{metal}/x_{FeO}^{silicate}$ for the reaction $FeO^{silicate} = Fe^{metal} + O^{metal}$. According to Tagawa et al.[4], the K_D^O values calculated without considering the presence of hydrogen and carbon are consistent with those obtained in the (H, C)-free system. It suggests that both hydrogen and carbon do not have colligative properties in iron solvent since small H and C atoms are incorporated into liquid Fe interstitially. Therefore, the activity of element i in metal is approximated as;

$$x_i' = \frac{N_i}{\sum_{k \neq H,C} N_k} \tag{10}$$

We obtained the mol-based D values from earlier experimental data with the same procedure.

First-principles calculations

First-principles calculations based on density functional theory were performed using the Quantum Espresso (QE) codes[69]. Generalized-gradient approximation[70] was adopted, along with projector-augmented wave (PAW) pseudopotentials available on the QE website (energy cutoff of 90 Ry). In our calculations, Fe_7C_3 (20-atom cells, $P6_3mc$ symmetry) with various site occupations of H were considered, including Wyckoff positions 2*a*, 2*b*, 6*c*, and 12 *d*. All considered structures are fully optimized (4×4×6 k-point mesh), and the results are fitted to the 3rd-order Birch–Murnaghan equation of state (Supplementary Table 5, Supplementary Fig. 13). For all considered structures, the ferromagnetic (FM) state is more favourable than the nonmagnetic (NM) state. As the H concentration increases, the favourable site occupations are $2a$, $2a + 2b$, and $2a + 6c$ for Fe_7C_3H, $Fe_7C_3H_2$, and $Fe_7C_3H_4$, respectively.

Data availability

The data to reproduce this paper is provided through https://zenodo.org/records/17357322. Any other original data are available from the corresponding author upon request.

Code availability

The codes to reproduce this paper are available at Code Ocean (https://doi.org/10.24433/CO.5580780.v1).

References

1. Alexander, C. M. O. et al. The provenances of asteroids, and their contributions to the volatile inventories of the terrestrial planets. *Science* **337**, 721–723 (2012).
2. Piani, L. et al. Earth's water may have been inherited from material similar to enstatite chondrite meteorites. *Science* **369**, 1110–1113 (2020).

3. Rubie, D. C. et al. Accretion and differentiation of the terrestrial planets with implications for the compositions of early-formed Solar System bodies and accretion of water. *Icarus* **248**, 89–108 (2015).
4. Tagawa, S. et al. Experimental evidence for hydrogen incorporation into Earth's core. *Nat. Commun.* **12**, 2588 (2021).
5. Fischer, R. A., Cottrell, E., Hauri, E., Lee, K. K. M. & Le Voyer, M. The carbon content of Earth and its core. *Proc. Natl. Acad. Sci. USA* **117**, 8743–8749 (2020).
6. Blanchard, I. et al. The metal–silicate partitioning of carbon during Earth's accretion and its distribution in the early solar system. *Earth Planet. Sci. Lett.* **580**, 117374 (2022).
7. Kuwayama, Y. et al. Equation of state of liquid iron under extreme conditions. *Phys. Rev. Lett.* **124**, 165701 (2020).
8. Hirose, K., Wood, B. & Vočadlo, L. Light elements in the Earth's core. *Nat. Rev. Earth Environ.* **2**, 645–658 (2021).
9. Marty, B. The origins and concentrations of water, carbon, nitrogen and noble gases on Earth. *Earth Planet. Sci. Lett.* **313-314**, 56–66 (2012).
10. Hirschmann, M. M. Constraints on the early delivery and fractionation of Earth's major volatiles from C/H, C/N, and C/S ratios. *Am. Miner.* **101**, 540–553 (2016).
11. Li, Y., Vočadlo, L., Sun, T. & Brodholt, J. P. The Earth's core as a reservoir of water. *Nat. Geosci.* **13**, 453–458 (2020).
12. Yuan, L. & Steinle-Neumann, G. Strong sequestration of hydrogen into the Earth's core during planetary differentiation. *Geophys. Res. Lett.* **47**, e2020GL088303 (2020).
13. Dasgupta, R., Chi, H., Shimizu, N., Buono, A. S. & Walker, D. Carbon solution and partitioning between metallic and silicate melts in a shallow magma ocean: implications for the origin and distribution of terrestrial carbon. *Geochim. Cosmochim. Acta.* **102**, 191–212 (2013).
14. Kuwahara, H., Itoh, S., Suzumura, A., Nakada, R. & Irifune, T. Nearly carbon-saturated magma oceans in planetary embryos during core formation. *Geophys. Res. Lett.* **48**, e2021GL092389 (2021).
15. Kuwahara, H., Itoh, S., Nakada, R. & Irifune, T. The effects of carbon concentration and silicate composition on the metal-silicate partitioning of carbon in a shallow magma ocean. *Geophys. Res. Lett.* **46**, 9422–9429 (2019).
16. Li, Y., Dasgupta, R., Tsuno, K., Monteleone, B. & Shimizu, N. Carbon and sulfur budget of the silicate Earth explained by accretion of differentiated planetary embryos. *Nat. Geosci.* **9**, 781–785 (2016).
17. Fichtner, C. E., Schmidt, M. W., Liebske, C., Bouvier, A.-S. & Baumgartner, L. P. Carbon partitioning between metal and silicate melts during Earth accretion. *Earth Planet. Sci. Lett.* **554**, 116659 (2021).
18. Wade, J. & Wood, B. J. Core formation and the oxidation state of the Earth. *Earth Planet. Sci. Lett.* **236**, 78–95 (2005).
19. Siebert, J., Badro, J., Antonangeli, D. & Ryerson, F. J. Metal–silicate partitioning of Ni and Co in a deep magma ocean. *Earth Planet. Sci. Lett.* **321**, 189–197 (2012).
20. Fischer, R. A. et al. High pressure metal–silicate partitioning of Ni, Co, V, Cr, Si, and O. *Geochim. Cosmochim. Acta.* **167**, 177–194 (2015).
21. Ma, Z. Thermodynamic description for concentrated metallic solutions using interaction parameters. *Metall. Mater. Trans. B* **32**, 87–103 (2001).
22. Siebert, J., Corgne, A. & Ryerson, F. J. Systematics of metal–silicate partitioning for many siderophile elements applied to Earth's core formation. *Geochim. Cosmochim. Acta.* **75**, 1451–1489 (2011).
23. Hirschmann, M. M. Comparative deep Earth volatile cycles: the case for C recycling from exosphere/mantle fractionation of major (H_2O, C, N) volatiles and from H_2O/Ce, CO_2/Ba, and CO_2/Nb exosphere ratios. *Earth Planet. Sci. Lett.* **502**, 262–273 (2018).
24. Lécuyer, C., Gillet, P. & Robert, F. The hydrogen isotope composition of seawater and the global water cycle. *Chem. Geol.* **145**, 249–261 (1998).
25. Peslier, A. H., Schönbächler, M., Busemann, H. & Karato, S.-I. Water in the Earth's interior: distribution and origin. *Space Sci. Rev.* **212**, 1–68 (2017).
26. Palme, H. & O'Neill, H. S. C. Cosmochemical estimates of mantle composition. In *Treatise on Geochemistry* 2nd edn, Vol. 3 (eds. Holland, H. D. & Turekian, K. K.) 1–39 (Elsevier, 2014).
27. McDonough, W. F. Compositional model for the Earth's core. In *Treatise on Geochemistry* 2nd edn, Vol. 3 (eds. Holland, H. D. & Turekian, K. K.) 559–577 (Elsevier, 2014).
28. Marty, B. et al. An evaluation of the C/N ratio of the mantle from natural CO_2-rich gas analysis: geochemical and cosmochemical implications. *Earth Planet. Sci. Lett.* **551**, 116574 (2020).
29. Takahashi, E. Melting of a dry peridotite KLB-1 up to 14 GPa: implications on the origin of peridotitic upper mantle. *J. Geophys. Res.* **91**, 9367–9382 (1986).
30. Siebert, J., Badro, J., Antonangeli, D. & Ryerson, F. J. Terrestrial accretion under oxidizing conditions. *Science* **339**, 1194–1197 (2013).
31. Wang, H. S., Lineweaver, C. H. & Ireland, T. R. The elemental abundances (with uncertainties) of the most Earth-like planet. *Icarus* **299**, 460–474 (2018).
32. Javoy, M. et al. The chemical composition of the Earth: enstatite chondrite models. *Earth Planet. Sci. Lett.* **293**, 259–268 (2010).
33. Umemoto, K. & Hirose, K. Chemical compositions of the outer core examined by first principles calculations. *Earth Planet. Sci. Lett.* **531**, 116009 (2020).
34. Hirose, K. et al. Crystallization of silicon dioxide and compositional evolution of the Earth's core. *Nature* **543**, 99–102 (2017).
35. Suer, T.-A., Siebert, J., Remusat, L., Menguy, N. & Fiquet, G. A sulfur-poor terrestrial core inferred from metal–silicate partitioning experiments. *Earth Planet. Sci. Lett.* **469**, 84–97 (2017).
36. Hirschmann, M. M., Bergin, E. A., Blake, G. A., Ciesla, F. J. & Li, J. Early volatile depletion on planetesimals inferred from C–S systematics of iron meteorite parent bodies. *Proc. Natl. Acad. Sci. USA* **118**, e2026779118 (2021).
37. Newcombe, M. E. et al. Degassing of early-formed planetesimals restricted water delivery to Earth. *Nature* **615**, 854–857 (2023).
38. Budde, G., Burkhardt, C. & Kleine, T. Molybdenum isotopic evidence for the late accretion of outer Solar System material to Earth. *Nat. Astron.* **3**, 736–741 (2019).
39. Fischer-Gödde, M. et al. Ruthenium isotope vestige of Earth's pre-late-veneer mantle preserved in Archaean rocks. *Nature* **579**, 240–244 (2020).
40. Burkhardt, C. et al. Terrestrial planet formation from lost inner Solar System material. *Sci. Adv.* **7**, eabj7601 (2021).
41. Dauphas, N., Hopp, T. & Nesvorný, D. Bayesian inference on the isotopic building blocks of Mars and Earth. *Icarus* **408**, 115805 (2024).
42. Deguen, R., Olson, P. & Cardin, P. Experiments on turbulent metal–silicate mixing in a magma ocean. *Earth Planet. Sci. Lett.* **310**, 303–313 (2011).
43. Lodders, K. Relative atomic solar system abundances, mass fractions, and atomic masses of the elements and their isotopes, composition of the solar photosphere, and compositions of the major chondritic meteorite groups. *Space Sci. Rev.* **217**, 44 (2021).
44. Wasson, J. T. & Kallemeyn, G. W. Compositions of chondrites. *Philos. T. R. Soc. A* **325**, 535–544 (1988).
45. Moore, C. B. & Lewis, C. F. The distribution of total carbon content in enstatite chondrites. *Earth Planet. Sci. Lett.* **1**, 376–378 (1966).
46. Alexander, C. M. O. Quantitative models for the elemental and isotopic fractionations in the chondrites: the non-carbonaceous chondrites. *Geochim. Cosmochim. Acta.* **254**, 246–276 (2019).
47. Alexander, C. M. O. Quantitative models for the elemental and isotopic fractionations in chondrites: the carbonaceous chondrites. *Geochim. Cosmochim. Acta.* **254**, 277–309 (2019).

48. Sakuraba, H., Kurokawa, H., Genda, H. & Ohta, K. Numerous chondritic impactors and oxidized magma ocean set Earth's volatile depletion. *Sci. Rep.* **11**, 20894 (2021).
49. Gu, J. T. et al. Composition of Earth's initial atmosphere and fate of accreted volatiles set by core formation and magma ocean redox evolution. *Earth Planet. Sci. Lett.* **629**, 118618 (2024).
50. Mashino, I., Miozzi, F., Hirose, K., Morard, G. & Sinmyo, R. Melting experiments on the Fe–C binary system up to 255 GPa: constraints on the carbon content in the Earth's core. *Earth Planet. Sci. Lett.* **515**, 135–144 (2019).
51. Hirao, N. et al. New developments in high-pressure X-ray diffraction beamline for diamond anvil cell at SPring-8. *Matter Radiat. Extrem.* **5**, 018403 (2020).
52. Helffrich, G. Outer core compositional layering and constraints on core liquid transport properties. *Earth Planet. Sci. Lett.* **391**, 256–262 (2014).
53. de Koker, N. P., Stixrude, L. & Karki, B. B. Thermodynamics, structure, dynamics, and freezing of Mg_2SiO_4 liquid at high pressure. *Geochim. Cosmochim. Acta.* **72**, 1427–1441 (2008).
54. Thibault, Y. & Walter, M. J. The influence of pressure and temperature on the metal-silicate partition coefficients of nickel and cobalt in a model C1 chondrite and implications for metal segregation in a deep magma ocean. *Geochim. Cosmochim. Acta.* **59**, 991–1002 (1995).
55. Akahama, Y. & Kawamura, H. High-pressure Raman spectroscopy of diamond anvils to 250 GPa: method for pressure determination in the multimegabar pressure range. *J. Appl. Phys.* **96**, 3748–3751 (2004).
56. Andrault, D. et al. Solidus and liquidus profiles of chondritic mantle: implication for melting of the Earth across its history. *Earth Planet. Sci. Lett.* **304**, 251–259 (2011).
57. Mori, Y. et al. Melting experiments on Fe–Fe_3S system to 254 GPa. *Earth Planet. Sci. Lett.* **464**, 135–141 (2017).
58. Fukai, Y. & Suzuki, T. Iron-water reaction under high pressure and its implication in the evolution of the Earth. *J. Geophys. Res.* **91**, 9222–9230 (1986).
59. Dorogokupets, P. I., Dymshits, A. M., Litasov, K. D. & Sokolova, T. S. Thermodynamics and equations of state of iron to 350 GPa and 6000. *K. Sci. Rep.* **7**, 41863 (2017).
60. Nakajima, Y. et al. Thermoelastic property and high-pressure stability of Fe_7C_3: implication for iron-carbide in the Earth's core. *Am. Mineral.* **96**, 1158–1165 (2011).
61. McGuire, C. et al. *P-V-T* measurements of Fe_3C to 117 GPa and 2100 K: implications for stability of Fe_3C phase at core conditions. *Am. Mineral.* **106**, 1349–1359 (2021).
62. Tagawa, S., Gomi, H., Hirose, K. & Ohishi, Y. High-temperature equation of state of FeH: implications for hydrogen in Earth's inner core. *Geophys. Res. Lett.* **49**, e2021GL096260 (2022).
63. Fischer, R. A. et al. Equations of state in the Fe-FeSi system at high pressures and temperatures. *J. Geophys. Res.* **119**, 2810–2827 (2014).
64. Tsutsumi, Y. et al. Retention of water in subducted slabs under core–mantle boundary conditions. *Nat. Geosci.* **17**, 697–704 (2024).
65. Yurimoto, H., Nagashima, K. & Kunihiro, T. High precision isotope micro-imaging of materials. *Appl. Surf. Sci.* **203–204**, 793–797 (2003).
66. Sakamoto, N. et al. Remnants of the early solar system water enriched in heavy oxygen isotopes. *Science* **317**, 231–233 (2007).
67. Greenwood, J. P. et al. Hydrogen isotope ratios in lunar rocks indicate delivery of cometary water to the Moon. *Nat. Geosci.* **4**, 79–82 (2011).
68. Shimizu, K. et al. H_2O, CO_2, F, S, Cl, and P_2O_5 analyses of silicate glasses using SIMS: report of volatile standard glasses. *Geochem. J.* **51**, 299–313 (2017).
69. Giannozzi, P. et al. Advanced capabilities for materials modelling with Quantum ESPRESSO. *J. Phys. Condens. Matter* **29**, 465901 (2017).
70. Perdew, J. P., Burke, K. & Ernzerhof, M. Generalized gradient approximation made simple. *Phys. Rev. Lett.* **78**, 1396 (1997).
71. Yokoyama, T. et al. Samples returned from the asteroid Ryugu are similar to Ivuna-type carbonaceous meteorites. *Science* **379**, eabn7850 (2023).
72. Lauretta, D. et al. Asteroid (101955) Bennu in the laboratory: properties of the sample collected by OSIRIS-REx. *Meteorit. Planet. Sci.* **59**, 2453–2486 (2024).

Acknowledgements

The authors acknowledge K. Yonemitsu for assisting with EPMA analyses. We thank S. Kawaguchi and H. Kadobayashi for their help in experiments at BL10XU, SPring-8 (proposal no. 2021B0181). We also thank S. Tagawa for his advice on melting experiments. This work was supported by the JSPS Kakenhi 21H04968 to K.H., 23KJ0479 to Y.T. and 21H04985 to H.Y. and by the "Imaging Platform" programme by MEXT. H.H. acknowledges support from the National Science and Technology Council of Taiwan under Grants No. NSTC 113-2116-M-008-010 and 114-2116-M-008-014-MY2.

Author contributions

Y.T. and K.H. designed and led the project. This study is based on DAC experiments by Y.T. and S.Y., SIMS analyses by N.S., H.Y. and Y.T., first-principles calculations by H.H. and computational modelling by Y.T., S.M. and S.Y. Y.T. and K.H. wrote the manuscript, and all authors commented on it.

Competing interests

The authors declare no competing interests.

Additional information

Supplementary information The online version contains supplementary material available at https://doi.org/10.1038/s41467-025-65729-5.

Correspondence and requests for materials should be addressed to Kei Hirose.

Peer review information *Nature Communications* thanks the anonymous reviewers for their contribution to the peer review of this work. A peer review file is available.